Hiroshima J. Med. Sci.
Vol. 67, No. 3, 63~69, September, 2018
HIMJ 67–11

Improved Detectability of Hyper-Dense Nodules Using Dual-Energy Computed Tomography Scanning: Phantom Study Using Simulated Liver Harboring Nodules

Enkhjargal BAYASGALAN, Toru HIGAKI, Wataru FUKUMOTO, Yuko NAKAMURA, Keigo CHOSA, Fuminari TATSUGAMI, and Kazuo AWAI*

Department of Diagnostic Radiology, Graduate School of Biomedical and Health Sciences, Hiroshima University, Hiroshima, Japan

ABSTRACT

The purpose of this study was to evaluate the detectability of hyper-dense nodules using dual-energy computed tomography (DECT) in a phantom. Arterial-phase hepatic dynamic computed tomography (CT) was conducted on small, medium, and large liver-simulating phantoms harboring simulated hypervascular tumors. We acquired 150 single-energy CT (SECT) and 150 DECT scans and measured the contrast-to-noise ratio (CNR) of the nodules. Alternative free response receiver observer characteristic (AFROC) curves of five radiologists' readings of the SECT and DECT scans were compared to assess detectability of the hyper-dense nodules. For all phantoms, the CNR of nodules measured using DECT was significantly higher than that by using SECT ($p < 0.001$, all). In the AFROC study, DECT showed a significantly larger area under the curve than that with SECT (0.778 vs 0.499, $p = 0.012$). Detectability of high-density nodules was better with DECT scans than with SECT scans.

Key words: *liver tumor, hyper-dense nodule, dual-energy CT, Phantom*

INTRODUCTION

The patients' body size and cardiac function, iodine mass of the contrast medium (CM) and its injection rate, and tube voltage and beam hardening artifacts affect arterial enhancement on computed tomography (CT) scans[3,20]. Beam hardening is a physical phenomenon that may affect organ enhancement on contrast-enhanced CT scans[5,24]. Schindera et al. performed *in vivo* and *in vitro* single-energy CT (SECT) studies and reported that beam hardening reduced the degree of arterial enhancement in large-bodied patients undergoing CT angiography[20]. Decreasing arterial enhancement by beam hardening may impair identification or characterization of lesions that show arterial enhancement on CT scans.

Hepatic hypervascular lesions are defined as lesions whose attenuation is higher than that of the surrounding liver parenchyma during arterial-phase dynamic CT[2]. Identification and characterization of the lesion are important for diagnosis and selection of appropriate treatment strategy[4,7,13]. In large-bodied patients, the intensity of the hypervascular liver lesions may be decreased due to beam hardening.

Recently clinically induced dual-energy CT (DECT) can reduce beam hardening artifact[16,25]. We hypothesized that conspicuity of hypervascular lesions was decreased due to beam hardening on SECT and DECT, could reduce beam hardening artifacts and improve lesion conspicuity. The purpose of this study was to investigate whether DECT could improve detectability of hyper-dense nodule in a phantom study.

MATERIALS AND METHODS

Phantoms simulating hypervascular tumors of the liver during the arterial phase of hepatic dynamic CT were prepared using a three-dimensional (3D) printer (Agilista 3200, Keyence, Osaka, Japan) (Figures 1A–C). The central body of the phantom was made of acrylate plastic with a CT number of approximately 60 HU through 120-kVp SECT imaging. Size of the central body was 300 × 200 mm in the axial plane (xy direction), and 50 mm along the z axis (Figure 1A), with 102 spherical holes of 10-mm diameter. A 3-mm-diameter columnar path connected the holes with the phantom's exterior (Figure 1B). To simulate the hyper-dense nodules, a solution containing iodine contrast medium (CM; Omnipaque-300, Daiichi-Sankyo, Tokyo, Japan) was injected into the paths through maximum three spherical holes that were arbitrarily chosen. CT number of the nodules was set as 10 HU higher than that of the phantom body with 120-kVp SECT imaging. Iodine concentration of the iodine solution was 300 mg/ml. The remaining holes were filled with sugar solution and the

* Corresponding author: Kazuo Awai
Department of Diagnostic Radiology, Graduate School of Biomedical and Health Sciences, Hiroshima University, 1-2-3 Kasumi, Minami-ku, Hiroshima 734-8551, Japan
E-mail: awai@hiroshima-u.ac.jp

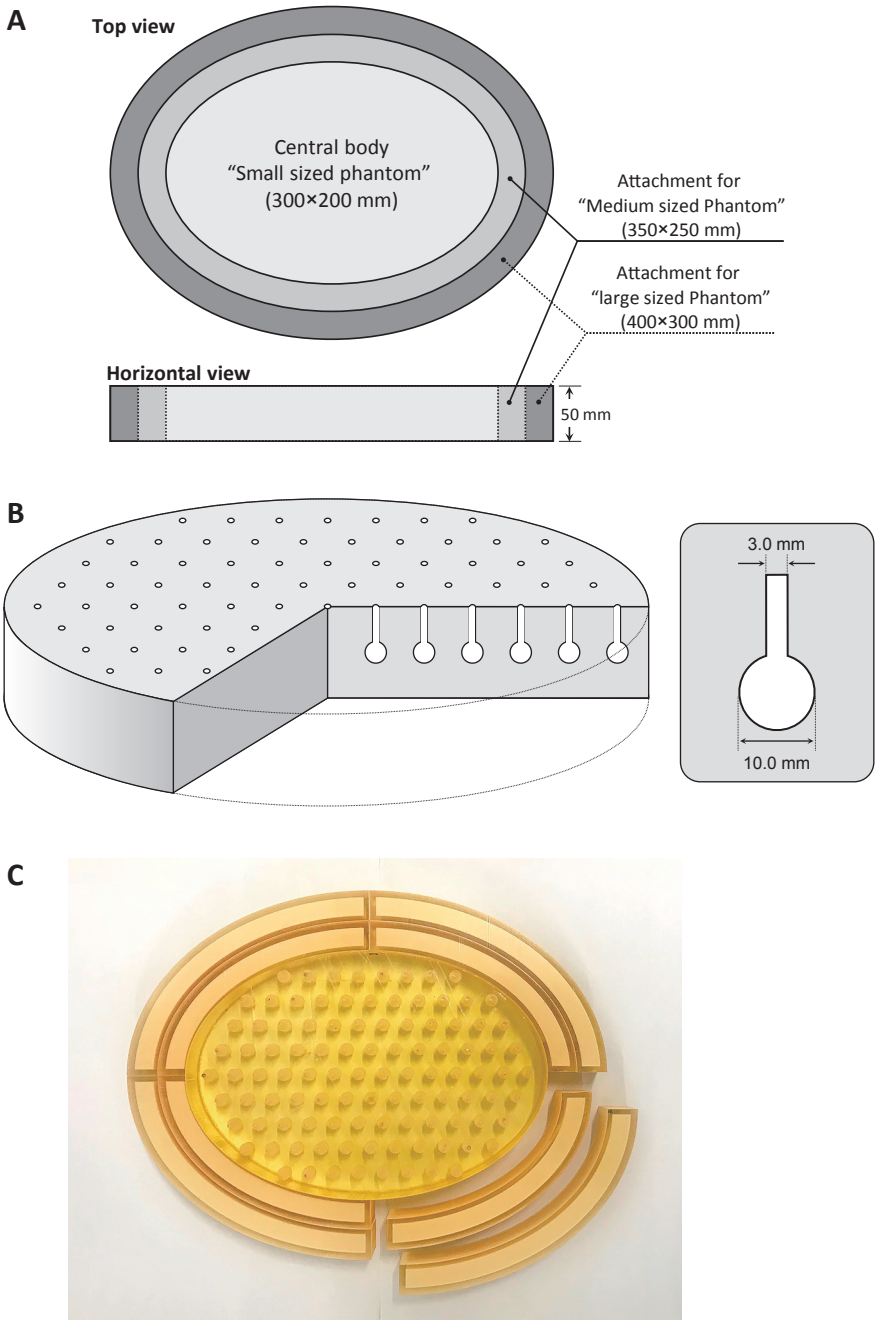

Figure 1 Configuration of the central body of the phantoms. A: The phantom (representative small phantom) consists of the central body (size in xy dimension, 300 × 200 mm; thickness, 50 mm). The phantom size was increased by encompassing the central body with 15-mm-wide frame made of the same material as that of the central body. B: Detailed structure of the central body of the phantom. The central body harbors 102 spherical holes (10-mm in diameter) to simulate the nodules. A 3-mm diameter columnar path allows for injection of CM to mimic the nodules. C: Photograph of the phantom showing the frames used to increase the phantom size.

CT number was adjusted to match that of the phantom body.

The central body was designated as the small phantom; central body with a frame of width, 15 mm, and outer diameter, 350 × 250 mm, as the medium phantom; and central body with a frame of width, 15 mm and outer diameter, 400 × 300 mm, as large phantom. Both frames were made of the same material as that of the central body (Figure 1A).

To mimic hyper-dense nodules, CM was injected into the paths through maximum three holes in the central body: one nodule in each of four bodies; two nodules in each of 12 bodies, and three nodules in each of 14 bodies (total, 70 nodules in 30 bodies); and 20 bodies were maintained as nodule-free. SECT and DECT scanning were performed in each phantom (small, medium, large).

CT scanning and image reconstruction

Phantoms were scanned using a 320-detector row CT scanner (Aquilion ONE ViSION Ed., Canon Medical Systems, Otawara, Japan). SECT scans were acquired at 120 kVp. DECT scanning was performed first at 80 kVp, and then at 135 kVp. For all scans, the volume scan mode (axial non-helical scan mode) was applied; and the

detector configuration for all scans was 80 × 0.5 mm.

For SECT scanning of a small phantom, the tube current was 85 mAs (170 mA and 0.5 sec/rotation), for a medium phantom, the settings were 175 mAs (350 mA and 0.5 sec/rotation), and for a large phantom, 250 mAs (250 mA and 1.0 sec/rotation). $CTDI_{vol}$ for small, medium, and large phantom was 8.2, 16.9, and 23.7 mGy, respectively. Preset image noise index was 12 in all phantoms.

For DECT scanning of the small phantom, the tube current second was set to the approximate value of $CTDI_{vol}$ as that for SECT scanning: 145 mAs at 80 kVp (290 mA and 0.5 sec/rotation) and 25 mAs at 135 kVp (50 mA and 0.5 sec/rotation). For medium phantom, the settings were 315 mAs at 80 kVp (630 mA and 0.5 sec/rotation) and 55 mAs at 135 kVp (110 mA and 0.5 sec/rotation); and for large phantom, 460 mAs at 80 kVp (460 mA and 1.0 sec/rotation) and 80 mAs at 135 kVp (80 mA and 1.0 sec/rotation). $CTDI_{vol}$ of DECT scan for small, medium, and large phantom was 8.0, 17.6, and 25.0 mGy, respectively.

From DECT scans, we generated virtual monochromatic 65-keV CT (VMCT) images corresponding to 120-kVp SECT images. Although our CT system has the capability to generate both image-based and projection-based VMCT images[25], we produced projection-based VMCT images. We reconstructed both scan data with hybrid iterative reconstruction [adaptive iterative dose reduction 3D (AIDR-3D, Canon Medical Systems, Otahara, Japan) with reconstruction kernel FC13 which is the standard kernel for abdominal CT.

Quantitative analysis of the phantom image

One radiologist with 4 years' experience with body CT imaging determined the CT number of the 70 hyper-dense nodules on SECT and DECT images. In addition, the CT number and standard deviation [SD] at four sites around each nodule were recorded. The region of interest (ROI) was maintained constant at approximately 50 mm^2. Mean CT number of the four sites was considered as the background CT number of the phantom and mean SD of those sites as the image noise. The contrast-to-noise ratio (CNR) of each nodule was calculated using the formula: CNR = [(CT number of the nodule) − (CT number of background)]/image noise.

Measurements were performed using Image J (https://imagej.nih.gov/ij/download.html). A gray-scale monitor (Model PA301A; NEC, Tokyo, Japan) with a spatial resolution of 2560 × 1600 was used for quantitative analysis.

Observer performance study

Five board-certified radiologists with 8–31 years' (median 17 years) experience with body CT imaging participated in the observer performance study; software used in the study was developed by one of the authors (TH). For operating the observer interface, five radiologists were trained on 12 images (nine with nodules, three without nodules). Training images were not included in actual observer performance study.

Readers were presented with total 300 images per single session [images of 30 phantoms with nodules plus 20 without nodules (50 images) × 2 modalities (SECT and DECT) × 3 (small, medium, large phantom)]. In total readings, there were four phantoms with one nodule, 12 phantoms with two nodules, and 14 phantoms with three nodules (30 phantoms with 70 nodules); and 20 phantoms without nodules (nodule-free). Observers first marked the location of hyper-dense nodules on each image by the click of a mouse. They then rated their confidence in their identification of the nodule(s) on the right side of the screen (Rating score, 100: definitely identified, and 0: definitely not identified). The images were presented in random order. The setting of window-level and screen-width was without restriction; in addition, no restrictions were placed on the reading time. Time to completion for each reading session was approximately 2 hr. We used the same gray-scale monitor as that for quantitative analysis of observer performance.

Statistical analysis

All numerical data are presented as the median and range. Wilcoxon signed-rank test and Medcalc version 18 (Medcalc Software bvba, Ostend, Belgium) were used to compare contrast and CNR on acquired DECT and SECT images of small, medium, and large phantoms. Jackknife alternative free-response ROC (JAFROC) analysis was performed to compare observer performance for detecting hyper-density nodules on images obtained through DECT and SECT. JAFROC analysis with multiple-reader multiple-case (MRMC) design considers the tumor location and allows the evaluation of multiple lesions on each image. For analysis of the MRMC-JAFROC data, we used DBM-MRMC software[6] provided by Chakraborty and Yoon (JAFROC 4.2.1, http://www.devchakraborty.com/index.php). AFROC curves were generated by plotting the lesion localization fraction against the false positive fraction, and area under the curve (AUC) was used as the figure of merit (FOM) for detectability of the hyper-dense nodules. Statistical tests were applied to all phantom data obtained through SECT and DECT. To avoid statistical errors due to multiple observations, we did not perform sub-analyses of findings from small, medium, and large phantoms[9]. Differences of $p < 0.05$ were recorded as statistically significant.

RESULTS

As shown in Table 1, on SECT and DECT images, the CNR of nodules decreased with the phantom size. The CNR on SECT scans of large phantoms was 85% lower than that of small phantoms; and on DECT images, it was 28.7% lower on those of large than small phantoms. For all three phantoms, the CNR of nodules measured through DECT was significantly higher than those through SECT ($p < 0.001$, all) (Figure 2).

AUC values for five observers are shown in Table 2, and the average of AFROC curves for detection of the hyper-dense nodules on SECT and DECT scans is shown

Table 1 Contrast to noise ratio (CNR) of simulated nodules and image noise

	Small sized phantom		Medium sized phantom		Large sized phantom	
	SECT	DECT	SECT	DECT	SECT	DECT
CNR of nodules	1.20 (0.46–2.78)	1.74 (0.55–2.90)	0.58 (–0.20–1.55)	1.41 (0.84–2.53)	0.18 (–0.56–1.22)	1.24 (0.07–1.92)
Image noise [HU]	6.2 (5.2–6.5)	6.7 (6.1–7.2)	7.4 (7.0–7.8)	7.5 (7.1–7.9)	9.3 (8.5–10.0)	8.5 (7.0–9.6)

Numbers indeicate median and numbesr in parenthesis indicate range
Abbriviation
SECT: single energy CT
DECT: dual energy CT

in Figure 3. The standard deviation of the AUC values for SECT and DECT was 0.14 and 0.07, respectively, which was relatively small (Table 2). In averaged AFROC curves for all observers, AUC value obtained with SECT and DECT for detection of the hyper-dense nodules was 0.50 and 0.77, respectively (Figure 3A); with a statistically significant difference (p = 0.012). In all (small, medium, and large) phantoms, AUC values for DECT were larger than that for SECT (Figures 3B–3D).

Representative phantom images are presented in Figures 4A–4F. For all three phantoms, the hyper-dense nodules were more clearly demonstrated on DECT images than on SECT images, with the large phantom was relatively small.

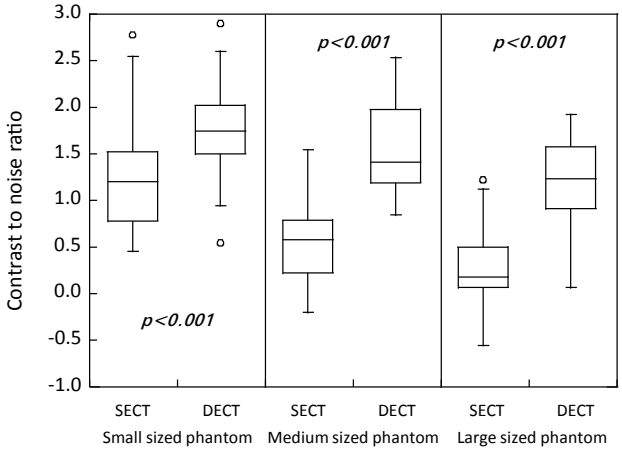

Figure 2 Comparison of CNR of the hyper-dense nodules on SECT and DECT scans of small, medium, and large phantom. For all phantoms, the CNR of nodules was significantly higher on the DECT scans than on the SECT scans (p < 0.001, all).

Table 2 AUC values of five observer in the alternative free response receiver operation charcteristics analysis (AFROC) study

Observer	AUC values	
	SECT	DECT
1	0.56	0.86
2	0.61	0.69
3	0.36	0.81
4	0.33	0.72
5	0.63	0.79
Mean (SD)	0.50 (0.14)	0.77 (0.07)

Abbreviation
SECT: single energy CT
DECT: dual energy CT
AUC: area under curve

DISCUSSION

Our study results indicated that CNR of the simulated hyper-dense nodules was higher on DECT images compared with that on SECT images irrespective of phantom size (p < 0.001); and AUC values for detection of the nodules were significantly higher with DECT than with SECT (p = 0.012). The findings indicated that DECT had superior performance over SECT for detection of the simulated hyper-dense nodule in phantom.

Beam hardening is a phenomenon whereby the mean energy of polychromatic X-ray increases with passage through tissue or media. Absorption of lower-energy photons in the spectrum is increased, which results in lowered attenuation of the beam per unit length[24]. Consequently, the CT number in the inner part of the body is lower than that in the outer part, also known as cupping artifact[5]. In this study, with SECT or DECT scanning, CNR of the hyper-dense nodule decreased as the size of phantom increased, possibly due to the enhancement of beam hardening effect through an increase in phantoms' size.

A correlated decrease in CNR with the increased size of the phantom was less with DECT than with SECT. We generated VMCT images through projection-based method. The main difference between projection- and image-based VMCT involves a method to determine the mass density of the two materials. For example, under DECT, two materials, such as water and iodine, are arbitrarily predetermined by radiologists to specify tissue components.

Application of projection-based method more effectively reduced beam-hardening artifact because beam hardening occurs in each X-ray projection[25]. In CT, under the condition of truly monochromatic X-ray, size of phantom shows no effect on CNR due to the absence of the beam hardening effect. However, on VMCT images through DECT, CNR showed a decrease as the phantoms' size increased, which suggested the persistence of post-correction residual artifact and requirement of a physical model (spectrum, detector, and imaging material)[14].

Other studies[1,10,11,17,19] that used CNR or signal-to-noise ratio (SNR) as the FOM reported that with DECT, conspicuity of the hypervascular tumors or iodine-

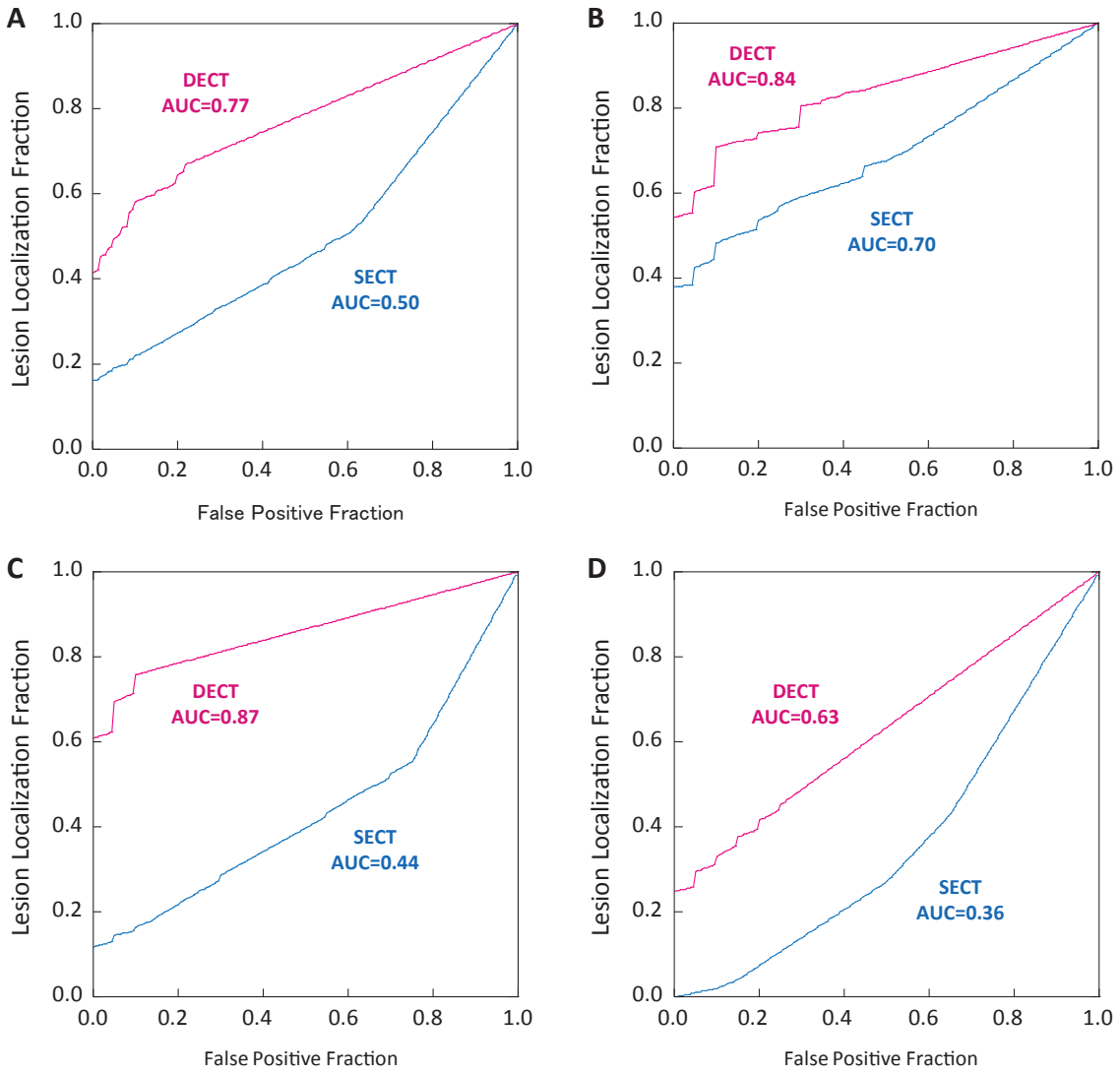

Figure 3 Averaged alternative free-response ROC curves for all observers tasked with detection of the hyper-dense nodules on SECT and DECT scans. A: All phantoms: Averaged AFROC curves for all observers. The AUC value was 0.50 for SECT and 0.77 for DECT (p = 0.012). B: Small phantom: Averaged AFROC curves for all observers. The AUC value was 0.70 for SECT and 0.84 for DECT. C: Medium phantom: Averaged AFROC curves for all observers. The AUC value was 0.44 for SECT and 0.87 for DECT. D: Large phantom: Averaged AFROC curves for all observers. The AUC value was 0.36 for SECT and 0.63 for DECT.

enhanced lesions could be improved. In contrast, in observer performance study, we used CNR and AUC through AFROC for comparative evaluation of SECT and DECT. As conspicuity of the liver tumor is affected by tumor-to-liver contrast[2,8,23] and image noise, CNR has become the index for tumor conspicuity[12,15,21,22]. However, the CNR is not always directly correlated with the diagnostic capability[12], since lesion conspicuity is affected by noise frequency. It is likely that in addition to CNR evaluation, ROC studies must be performed to confirm the lesions' detectability in a clinical setting.

Our findings suggested that detectability of the hypervascular liver tumors can be improved by obtaining VMCT images, especially in patients with larger abdominal circumference. Image acquisition may greatly improve detection of the hypervascular liver tumors not only in obese patients but also in patients with complications of massive ascites accompanied cirrhosis due to hepatocellular carcinoma. Likewise, metastatic liver tumors can be accompanied by massive ascites due to carcinomatous peritonitis, resulting in enlargement of the abdominal circumference that may impair detection of the hypervascular liver tumors.

In this study, we used simulated nodules of 10-mm diameter and adjusted the nodules' CT number as 10 HU higher than CT number of the phantom body. In a clinical case of hypervascular hepatocellular carcinoma, Yanaga et al. reported a 95% confidence interval of the tumor-to-liver contrast of 17.3–25 HU[23]. We conducted a phantom study under conditions of homogeneous background of the phantom, the presence of fewer artifacts compared to that in a clinical setting, and CT number of 10-HU difference between the simulated nodules and background. Moreover, we adopted a nodule diameter of 10 mm per American College of Radiology LI-RADS (https://www.acr.org/Clinical-Resources/Reporting-and-Data-Systems/LI-RADS/CT-MRI-LI-RADS-v2017) guideline with regard to minimum value requirement for characterizing arterial phase hyper-enhancement.

Our study has some limitations. We generated the

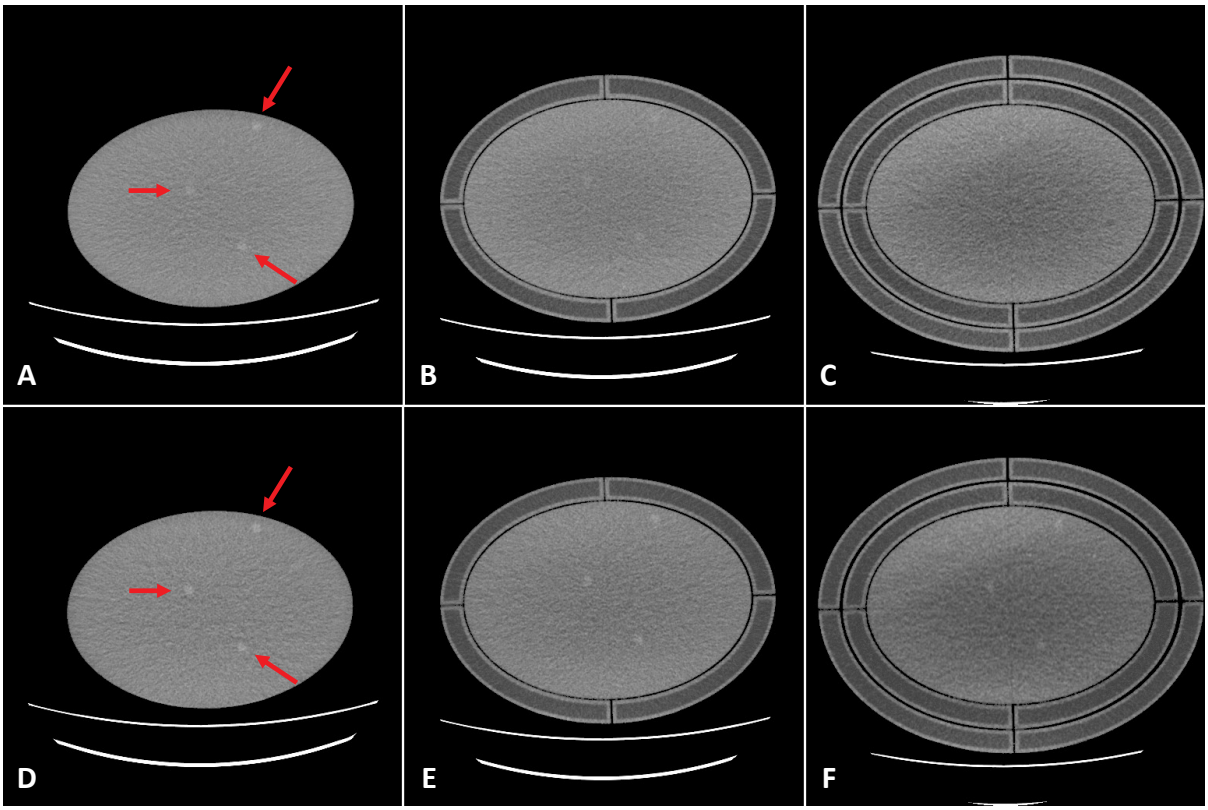

Figure 4 CT images of the phantoms. A: SECT: Small phantom. B: SECT: Medium phantom. C: SECT: Large phantom. D: DECT: Small phantom. E: DECT: Medium phantom. F: DECT: Large phantom. Arrows indicate hyper-dense nodules consisting of a solution of iodine contrast media. In all three phantoms, the hyper-dense nodules were more clearly demonstrated on DECT than SECT images.

VMCT images at constant 65 keV from the DECT data. Although specific keV values yield the lowest image noise and the highest CNR through different DECT scanners[15,17,18,25], Mileto et al.[19] reported that optimal monochromatic energy level for maximizing conspicuity of the hypervascular liver tumors was significantly affected by the patients' body habitus. They reported that higher keV levels are optimal for use in the study of a large phantom. Based on these reports, the selection of different keV according to the size of the phantom might be preferable. Second, the 50-mm thickness of phantom may have been inadequate because total detector width of the CT scanner was 40 mm at isocenter of the X-ray. Consequently, X-ray scatter may have affected our results.

In conclusion, in this phantom study to mimic the arterial phase of dynamic CT imaging of the liver, DECT showed superior performance over SECT in the detection of the hyper-dense nodules simulating hypervascular liver tumors. Future clinical studies to confirm our preliminary observation is planned.

Summary

Based on the results from this phantom study, we concluded that DECT was superior to SECT as a detection method of the hyper-dense nodules simulating hypervascular liver tumors. The limitations of our study include the use of generated VMCT images at constant 65 keV from DECT data and 50-mm thickness of the phantom. Clinical studies are required to confirm observations through the present phantom study.

(Received May 31, 2017)
(Accepted June 15, 2018)

REFERENCES

1. Altenbernd, J., Heusner, T.A., Ringelstein, A., Ladd, S.C., Forsting, M. and Antoch, G. 2011. Dual-energy-CT of hypervascular liver lesions in patients with HCC: investigation of image quality and sensitivity. Eur. Radiol. 21: 738–743.
2. Awai, K., Takada, K., Onishi, H. and Hori, S. 2002. Aortic and hepatic enhancement and tumor-to-liver contrast: analysis of the effect of different concentrations of contrast material at multi-detector row helical CT. Radiology. 224: 757–763.
3. Bae, K.T. 2010. Intravenous contrast medium administration and scan timing at CT: considerations and approaches. Radiology. 256: 32–61.
4. Baron, R.L. 1994. Understanding and optimizing use of contrast material for CT of the liver. AJR Am. J. Roentgenol. 163: 323–331.
5. Barrett, J.F. and Keat, N. 2004. Artifacts in CT: recognition and avoidance. Radiographics. 24: 1679–1691.
6. Dorfman, D.D., Berbaum, K.S. and Metz, C.E. 1992. Receiver operating characteristic rating analysis. Generalization to the population of readers and patients with the jackknife method. Invest. Radiol. 27: 723–731.
7. European Association For The Study Of The L, European Organisation For R, Treatment Of C. 2012. EASL-

EORTC clinical practice guidelines: management of hepatocellular carcinoma. J. Hepatol. 56: 908–943.
8. Furlan, A., Marin, D., Vanzulli, A., Patera, G.P., Ronzoni, A., Midiri, M., et al. 2011. Hepatocellular carcinoma in cirrhotic patients at multidetector CT: hepatic venous phase versus delayed phase for the detection of tumour washout. Br. J. Radiol. 84: 403–412.
9. Gonen, M., Panageas, K.S. and Larson, S.M. 2001. Statistical issues in analysis of diagnostic imaging experiments with multiple observations per patient. Radiology. 221: 763–767.
10. Grosse, H.N., Hoink, A.J., Doerner, J., Jordan, D.W., Pahn, G., Persigehl, T., et al. 2017. Assessment of arterially hyper-enhancing liver lesions using virtual monoenergetic images from spectral detector CT: phantom and patient experience. Abdom. Radiol. (NY). Nov 28. [Epub ahead of print]
11. Husarik, D.B., Gordic, S., Desbiolles, L., Krauss, B., Leschka, S., Wildermuth, S., et al. 2015. Advanced virtual monoenergetic computed tomography of hyperattenuating and hypoattenuating liver lesions: ex-vivo and patient experience in various body sizes. Invest. Radiol. 50: 695–702.
12. Jensen, K., Andersen, H.K., Tingberg, A., Reisse, C., Fosse, E. and Martinsen, A.C. 2016. Improved Liver Lesion Conspicuity With Iterative Reconstruction in Computed Tomography Imaging. Curr. Probl. Diagn. Radiol. 45: 291–296.
13. Kudo, M., Izumi, N., Kokudo, N., Matsui, O., Sakamoto, M., Nakashima, O., et al. 2011. Management of hepatocellular carcinoma in Japan: Consensus-Based Clinical Practice Guidelines proposed by the Japan Society of Hepatology (JSH) 2010 updated version. Dig. Dis. 29: 339–364.
14. Kyriakou, Y., Meyer, E., Prell, D. and Kachelriess, M. 2010. Empirical beam hardening correction (EBHC) for CT. Med. Phys. 37: 5179–5187.
15. Leng, S., Yu, L., Fletcher, J.G. and McCollough, C.H. 2015. Maximizing Iodine Contrast-to-Noise Ratios in Abdominal CT Imaging through Use of Energy Domain Noise Reduction and Virtual Monoenergetic Dual-Energy CT. Radiology. 276: 562–570.
16. Marin, D., Boll, D.T., Mileto, A. and Nelson, R.C. 2014. State of the art: dual-energy CT of the abdomen. Radiology. 271: 327–342.
17. Marin, D., Ramirez-Giraldo, J.C., Gupta, S., Fu, W., Stinnett, S.S., Mileto, A., et al. 2016. Effect of a Noise-Optimized Second-Generation Monoenergetic Algorithm on Image Noise and Conspicuity of Hypervascular Liver Tumors: An In Vitro and In Vivo Study. AJR Am. J. Roentgenol. 206: 1222–1232
18. Matsumoto, K., Jinzaki, M., Tanami, Y., Ueno, A., Yamada, M. and Kuribayashi, S. 2011. Virtual monochromatic spectral imaging with fast kilovoltage switching: improved image quality as compared with that obtained with conventional 120-kVp CT. Radiology. 259: 257–262.
19. Mileto, A., Nelson, R.C., Samei, E., Choudhury, K.R., Jaffe, T.A., Wilson, J.M., et al. 2014. Dual-energy MDCT in hypervascular liver tumors: effect of body size on selection of the optimal monochromatic energy level. AJR Am. J. Roentgenol. 203: 1257–1264.
20. Schindera, S.T., Tock, I., Marin, D., Nelson, R.C., Raupach, R., Hagemeister, M., et al. 2010. Effect of beam hardening on arterial enhancement in thoracoabdominal CT angiography with increasing patient size: an in vitro and in vivo study. Radiology. 256: 528–535.
21. Shuman, W.P., Green, D.E., Busey, J.M., Kolokythas, O., Mitsumori, L.M., Koprowicz, K.M., et al. 2013. Model-based iterative reconstruction versus adaptive statistical iterative reconstruction and filtered back projection in liver 64-MDCT: focal lesion detection, lesion conspicuity, and image noise. AJR Am. J. Roentgenol. 200: 1071–1076.
22. Shuman, W.P., Green, D.E., Busey, J.M., Mitsumori, L.M., Choi, E., Koprowicz, K.M., et al. 2014. Dual-energy liver CT: effect of monochromatic imaging on lesion detection, conspicuity, and contrast-to-noise ratio of hypervascular lesions on late arterial phase. AJR Am. J. Roentgenol. 203: 601–606.
23. Yanaga, Y., Awai, K., Nakaura, T., Namimoto, T., Oda, S., Funama, Y., et al. 2008. Optimal contrast dose for depiction of hypervascular hepatocellular carcinoma at dynamic CT using 64-MDCT. AJR Am. J. Roentgenol. 190: 1003–1009.
24. Young, S.W., Muller, H.H. and Marshall, W.H. 1983. Computed tomography: beam hardening and environmental density artifact. Radiology. 148: 279–283.
25. Yu, L., Leng, S. and McCollough, C.H. 2012. Dual-energy CT-based monochromatic imaging. AJR Am. J. Roentgenol. 199 (5 Suppl): S9–S15.